https://doi.org/10.1016/j.actamat.2017.07.029

Heterogeneous precipitation behavior and stacking-fault-mediated deformation in a CoCrNi-based medium-entropy alloy

Y. L. Zhao[a], T. Yang[a], Y. Tong[a,b,*], J. Wang[a,b], J.H. Luan[a,c], Z.B. Jiao[d], D. Chen[a], Y. Yang[a], A. Hu[a,b], C.T. Liu[a,c], J.-J. Kai[a,b,*]

a Department of Mechanical and Biomedical Engineering, City University of Hong Kong, Hong Kong, China

b Centre for Advanced Nuclear Safety and Sustainable Development, City University of Hong Kong, Hong Kong, China

c Center for Advanced Structural Materials, Department of Mechanical and Biomedical Engineering, City University of Hong Kong, Hong Kong, China

d Department of Mechanical Engineering, The Hong Kong Polytechnic University, Hong Kong, China

Abstract

Combining high strength and good ductility is highly-desired yet challenging for conventional structural materials. Newly emerging concentrated multi-component alloys with face-centered-cubic structure provide an ultra-ductile matrix, and the precipitation hardening based on these alloys provides a very effective way to achieve a superior strength-ductility combination. Here, we report a high-strength CoCrNi-based medium-entropy alloy hardened by nanoscale L12-(Ni, Co, Cr)3(Ti, Al)-type particles with mixing heterogeneous and homogeneous precipitation behaviors. Compared to the single-phase CoCrNi medium-entropy alloy, the yield strength and the tensile strength of the precipitation- strengthened CoCrNi medium-entropy alloy were increased by ~70% to ~750 MPa and ~44% to ~1.3 GPa, respectively, whereas a good ductility, ~45%, was still achieved. The underlying deformation micro-mechanisms were systematically investigated using transmission electron microscope. In the single-phase CoCrNi medium-entropy alloy, the deformation mode was dominated by mechanical twinning. In the precipitation-hardened medium-entropy alloy, however, a

high density of stacking faults prevailed. We revealed that the absence of mechanical twinning in this low stacking fault energy precipitation-strengthened medium-entropy alloy could relate to the increasing critical twinning stress affected by the channel width of the matrix. We further calculated that the increment of the yield strength was substantially from precipitation strengthening. Our present findings provide not only a fundamental understanding of the deformation micro-mechanism of the precipitation-strengthened CoCrNi medium-entropy alloy but also a useful guidance for the development of precipitation- hardened concentrated multi-component alloys in the future.

1. Introduction

High entropy alloys (HEAs) or concentrated multi-component alloys (CMCAs) are currently receiving extensive attentions from the materials science community [1], [2], [3], [4], [5], [6], particularly the HEAs with single face-centered-cubic (fcc) structure, due to their superior properties, such as excellent ductility [7], good corrosion resistance [8] and high radiation tolerance [9]. However, in regard to engineering application, the ductility of these single-fcc HEAs is often surplus while their strength, especially the yield strength, is generally insufficient at room temperature. Consequently, an appropriate design is highly demanded for these single-fcc HEAs to attain a superior combination of high strength and good ductility.

Precipitation hardening has been proved to be a very effective mechanism to improve the strength of HEAs. He et al. reported a FeCoNiCr-based HEA strengthened with coherent nanoscale L12 particles, resulting in a high tensile strength of ∼1.3 GPa and a good tensile elongation of 17% [10]. More interestingly, for a FeCoNiCrMo0.3

HEA strengthened by brittle intermetallics, a ductility of ~19% was still obtained at high strength level [11]. The reason for the good ductility obtained in these precipitate-hardened HEAs is twofold. One is the low stacking fault energy (SFE) of the HEA matrix [12], leading to increased twinning capability for ductility promotion, namely the twining-induced plasticity (TWIP) effect. The other is that the ductile fcc matrix exhibits a high work hardening capability during deformation, which can effectively suppress the propagation of micro-cracks [11]. Noticeably, compared with the four-component or five-component single-phase fcc HEAs, the three-component CoCrNi medium-entropy alloy (MEA) exhibits high work hardenability and excellent ductility [13]. It is therefore reasonable to expect that this three-component CoCrNi MEA can be a superior base alloy for precipitation hardening. Unfortunately, current investigations are mainly focused on the deformation behavior of the single-phase fcc CoCrNi MEA, including microstructure evolution with strain, the critical twinning stress and three dimension (3D) twinning architecture [14], [15], no endeavor has been made in the precipitation-hardened CoCrNi-based MEA. In addition, it remains an open question about how the precipitates influence the deformation micro-mechanisms of matrix.

In this work, a small amount of Al and Ti, strong gamma-prime phase (γ') formers [16], were added into the CoCrNi matrix in order to introduce precipitates. The precipitation behavior, including size and density, morphology and composition of the second-phase particles, was carefully characterized. Meanwhile, the strengthening and deformation micro-mechanisms activated in this precipitation-hardened MEA were systematically investigated and discussed based on the observations from transmission electron microscope(TEM).

2. Experimental details

The alloy with a nominal composition of (CoCrNi)94Al3Ti3 (denoted as Al3Ti3 MEA hereafter) was produced by arc-melting a mixture of high-purity raw elements (>99.9% pure) in a Ti-gettered argon atmosphere. The ingot was flipped and remelted five times to promote chemical homogeneity, and then dropped into a rectangular cross-section copper mould with a dimension of 5 × 10 × 100 mm3. The as-cast alloy was first solution-treated at 1200 °C for 2 h and then cold rolled along the longitudinal direction with a total thickness reduction of ~66%, followed by annealing at 1160 °C for 3 min leading to an equiaxed grain structure with ~67 μm grain size. Subsequently, the recrystallized sheet was isothermally aged at 800 °C for 2 h. All the heat treatment was conducted in air, followed by water quenching. The three-component CoCrNi alloy with a single-phase fcc structure (denoted as CoCrNi MEA hereafter) was also prepared for comparison, exhibiting an equiaxed grain structure with an average grain size of ~6.5 μm.

Dog-bone-shaped specimens with a gauge length of 12.5 mm and a cross-section of 3.2 × 1.5 mm2 were fabricated by electro-discharge machining for tensile test. Both sides of the specimens were carefully ground to 2500 grit finish using SiC paper. The uniaxial tensile tests were performed on a Material Testing System (MTS, Alliance RT30) tension machine at ambient temperature with an engineering strain rate of 1 × 10−3 s−1. The microhardness measurements were carried out in a Vicker Hardness tester with a nominal load of 1.5 N and a dwell time of 15 s. The hardness value was an average of ten tests.

Phase identification was conducted on X-ray diffractometer (XRD, Rigaku) equipped with a monochromator. Microstructure characterization was carried out via scanning

electron microscope (SEM, Quanta FEG450) and transmission electron microscope operating under 200 keV (TEM, JEOL 2100F). For the SEM analysis, in order to investigate the overall precipitation behavior, the aged samples were metallographically polished and then chemically etched with a dilute aqua regia solution. For the TEM investigation, the sheet specimens were firstly mechanically ground to a thickness below 100 μm using SiC paper, then punched into 3-mm-diameter discs and further thinned by ion-milling to a thickness of electron transparency. To study the effect of precipitation on the deformation modes, interrupted tensile tests stopped at different strains were conducted. Afterwards, the gauge length section of the deformed specimens was processed for TEM observations. The elemental distribution was studied using energy-dispersive X-ray spectroscopy (EDX) equipped in TEM and atom probe topography (APT). Needle-shaped specimens required for APT were fabricated by lift-outs and annular milled in a FEI Scios focused ion beam/scanning electron microscope (FIB/SEM). The APT characterization was performed in a local electrode atom probe (CAMEACA LEAP 5000 R). The APT specimens were analyzed at 70 K in voltage mode, with a pulse repetition rate of 125 KHz, a pulse fraction of 15%, and an evaporation detection rate of 0.2% atom per pulse. Imago Visualization and Analysis Software (IVAS) in version 3.6.12 was used for 3D reconstruction and composition analysis.

3. Results and discussion

3.1. Microstructures and elemental distribution

XRD pattern of the Al3Ti3 MEA is presented in Fig. 1 a. The characteristic peaks of fcc structure can be clearly identified, identical to those of the CoCrNi MEA [14]. The missing superlattice peaks from the second-phase precipitates may be due to peak

broadening effect from nano-sized precipitates and a small scattering-factor difference due to the complicate atomic occupation in the ordered phase [17]. Fig. 1b shows the corresponding SEM micrograph of the Al3Ti3 MEA, revealing a significantly heterogeneous precipitation behavior. Non-uniform growth of discontinuous precipitation (DP) colonies from grain boundaries was frequently observed. Under the present aging condition, the growth of DP colonies consumes the matrix on both sides of the initial grain boundaries to form a typical double-seam morphology and the volume fraction of the DP colonies is estimated to be ~60%. A representative high magnification image of the boundary (namely, reaction front) between the DP colony and inner grain is presented in Fig. 1c. Unlike an ideal DP reaction showing a lamellar structure alternated by matrix and precipitation through the whole DP colony [18], the size and morphology of the precipitates in the DP colonies of the Al3Ti3 MEA vary greatly. A close view of the discontinuous precipitates in a DP colony of the Al3Ti3 MEA through the bright-field (BF) and dark-field (DF) TEM imaging is shown in Fig. 2 a and b. In addition to the relatively large lamellar-like precipitates near the reaction front, some fine short-rods or even spherical precipitates were also observed away from the reaction front (near the original grain boundary). In contrast, a continuous precipitation (CP) behavior in the inner grain (denoted as CP region hereafter) was observed by BF and DF techniques via TEM. In Fig. 2c and d, a group of spherical particles with an average size of 10 nm are uniformly distributed in the inner grains. Inspection of the selected area diffraction patterns (SADPs) from three different Zone-axes (Fig. 2e and the inset in Fig. 2c) confirms that the matrix has a fcc structure (γ phase), whilst the additional faint points reveal that the precipitates both in the CP region and DP colonies have a superlattice L12 structure (γ' phase). Furthermore, the interfaces between the matrix and two types of precipitates (lamellar and spherical) are

shown in Fig. 2f and g, respectively. Coupled with the corresponding Fast Fourier transformation (FFT) images, we can see that the precipitates and the matrix are interfacially coherent.

As shown in Fig. 2, γ′ precipitates in the Al3Ti3 MEAs can be formed either continuously or discontinuously. Generally, CP and DP reactions are competitive and DP reaction is usually confined to grain boundary region [19]. In an early suggestion, a high precipitate-matrix lattice misfit (>1%), 11% solute-solvent size mismatch or a high decrease in grain-boundary energy due to solute segregation could be prerequisite for DP [18]. In our case, the precipitate-matrix lattice misfit should be rather small (Fig. 2f and g) and the atomic mismatch (∼4%) is below the criterion, so only grain boundary segregation by Ti or Al might be responsible for the occurrence of DP reaction. High-energy grain boundaries are preferred nucleation sites for γ′ phase, and the growth of the γ′ phase requires grain boundary migration towards the solute supersaturated matrix. With the moving grain boundary, an aggregate of γ′ phase and residual γ phase, stacked edgewise in alternating sequence, was formed and aligned normal to the reaction front. The formation of the rod and spherical particles might be a consequence of Rayleigh instability [20], [21], which is similar to the DP reaction in Co-Cu alloy [22].

Fig. 3 shows the STEM-EDX mapping results of a DP colony. The precipitates in the DP region are enriched with Ni, Al and Ti while keep a relatively low concentration of Co and Cr. Due to the small size of γ′ phase in the CP region, determination of the chemical composition of γ′ phase via STEM-EDX technique can dramatically disturbed by the signal from the matrix. In order to quantitatively reveal the elemental partitioning on the atomic scale, needle tips lifted out from the CP region were analyzed by APT. Fig. 4 a shows the typical atom map of all elements in the CP region. A 10 at.% Ti

iso-concentration surface is also displayed to delineate the outline of the precipitates in the CP region. The average size of the precipitates is about 10 ± 2 nm, consistent with the TEM observation (Fig. 2). The number density of the precipitates is approximately 2 × 1023/m3 and the volume fraction is ~11 ± 6%. The composition analysis was analyzed by a mean of proximity histogram (proxigram) calculated from the iso-concentration surfaces (Fig. 4b). The elemental distribution of each phase in the CP and DP regions is summarized in Table 1 . We can see that the elemental partitioning behavior is almost identical in both CP (Fig. 3) and DP regions (Fig. 4). Ni, Al and Ti have a very strong tendency to partition into the L12 nanoparticles, whilst Co is partially depleted and Cr is largely depleted from the nanoparticles. In general, Co and Cr can be substituted for the Ni sites, and Al and Ti occupy the same lattice sites. Thus, these nanoparticles can be identified as the (Ni, Co, Cr)3(Ti, Al) phases.

Phase stability of the complex (CoCrNi)97-xTi3-Alx alloy system was evaluated by CALPHAD (CALculation of PHAse Diagrams) method [23]. Fig. 5 shows the calculated equilibrium phase diagram and the equilibrium phase fractions as a function of temperature. The Al3Ti3 MEA is marked as red dashed line (Fig. 5a). As exhibited in the calculation, a two-phase region, consisting of equilibrium γ and γ′ phases, only exists in a narrow temperature range from 940 °C to 980 °C. However, in the present work, this two-phase region is also observed after aging at 800 °C (Fig. 2), where a small mole fraction of σ phase should be formed by consuming the fcc matrix (Fig. 5b). CALPHAD-based phase diagram calculation has been proved to be a feasible and reliable tool to evaluate the phase stability of multicomponent alloy system [11], [24], [25]. Two possibilities may account for the discrepancy between the prediction and the experimental results. For the calculation itself, its reliability and accuracy depends greatly on the available thermodynamic database, which, however,

is patchy and incomplete for the multi-component alloy system. On the other hand, the present Al3Ti3 MEA may not reach an equilibrium within a 2 h aging period due to a slow kinetics of forming σ phase. The evaluation of the equilibrium phases especially after a prolonged aging time will be included in our future work.

3.2. Mechanical properties under tensile deformation

The mechanical response of the Al3Ti3 MEA was examined under uniaxial tensile test. More than three samples were tested and one representative engineering stress-strain curve was plotted in Fig. 6 a. To reveal the effect of second-phase L12 nanoparticles on the mechanical performance of the Al3Ti3 MEA, the tensile result of the single-phase CoCrNi MEA is also presented. Compared to the CoCrNi MEA, the Al3Ti3 MEA exhibits a striking improvement in the mechanical performance by increasing the yield strength from ~430 MPa to ~750 MPa (~70%) and the ultimate tensile strength from ~900 MPa to ~1.3 GPa (~44%) while maintaining a high elongation, 45%. Apparently, a good combination of high strength and good ductility can be readily achieved in this precipitation-strengthened MEA.

Fig. 6b illustrates the work hardening behavior of these two MEAs as a function of true strain. The work hardening rate of both alloys drops steeply at the early stage of the plastic deformation and then slowly decreases as the strain further increases. It is also noticeable that the Al3Ti3 MEA has a much higher work hardening capability than the single-phase CoCrNi MEA during the entire plastic deformation. The enhancement of working hardening rate can be ascribed to the introduction of the second-phase precipitates, which can pin the dislocations and accordingly promote the dislocation accumulation for strain hardening. Fig. 6c compares the ultimate tensile strength and

elongation of the present alloy with various commercial superalloys[26], including solid-solution-hardened (SSH) superalloys and precipitation-hardened (PH) superalloys. A normal strength-ductility tradeoff can be apparently seen for the most superalloys. In contrast, our newly developed MEA does exhibit an excellent combination of strength and ductility, making it a promising alternative for high-temperature applications. Certainly, the mechanical performance can be further improved by carefully tailoring the alloy composition and optimizing the heat-treatment condition, and a systematical study will be shown in the future. In our present work, we will mainly focus on the influence of heterogeneous precipitates on the plastic deformation mechanism in the CoCrNi MEA. In the following sections, deformed specimens from additional interrupted tests (indicated by grey stars in Fig. 6a) were analyzed by TEM.

3.3. Evolution of deformation substructure in Al3Ti3 MEA

For a material strengthened by coherent ordered precipitates, the deformation behavior highly depends on the size of the precipitates. For example, with an increase of the γ′ precipitation size in a Co-rich nickel-based superalloy, the deformation mode changes from anti-phase boundary (APB) shearing by 1/2〈110〉dislocation pairs to stacking fault (SF) shearing by 1/6<112〉partial dislocations to Orowan bypassing [27], [28]. In our Al3Ti3 MEA, all of the above situations may be simultaneously present. Fig. 7 shows a typical deformation microstructure of the Al3Ti3 MEA deformed to ∼2% true strain. The dislocation structure at this deformation stage is characterized by multiple planar slip along two {111} slip planes. The average spacing between the criss-crossing active planes is ∼200 nm. Such a situation is expected to arise if the SFE of the alloy is sufficiently low to inhibit cross slip. Moreover, the existence of short range order (SRO) in matrix or ordered precipitates with a long range order (LRO) structure

also promotes the slip planarity [29]. Additionally, the SF fringes and pair-wise dislocations observed in the CP region (Fig. 7b) suggest that the γ′ ordered precipitates are deformed by either SF shearing or APB shearing (inset in Fig. 7b). In DP colonies, the precipitation size varies to a great extent. Nevertheless, both small spherical (Fig. 7c) and large lamellar-like (Fig. 7d) precipitates are all sheared by SFs. No evidence of Orowan loops around the γ′ precipitates could be found.

As deformation continues, SFs start to serve as an additional carrier of plasticity and interact with each other to divide the CP region into blocks (Fig. 8 a). Mechanical twinning was not found in the CP region, confirmed by the absence of twinning reflections in the SADP (see inset in Fig. 8a). Fig. 8c shows a typical microstructural image of the DP region at the same strain. Likewise, SFs also serve as a major carrier of plasticity in the DP regions (see inset in Fig. 8c and d). We also found that SFs were activated in two {111} planes in the CP region (Fig. 8a) but almost extended in one direction in the DP region (Fig. 8c), which could be related to the difference of precipitation morphology in these two regions. Fig. 9 shows other microstructural features containing some band-like structure (Fig. 9c) in the DP region. From the STEM images in Fig. 9c, we can see that the band-like structures are confined by two arrays of precipitates. Within those bands, a high density of SFs together with rare micro-twins can be observed (Fig. 9b). After a sampling of 400 sites in four grains, we found that only 2.5% of the sampled sites had micro-twins while the rest sites showed SFs although pervasive partial dislocation activities were known to be a prerequisite for twin nucleation [30]. In conclusion, the deformation process in our Al3Ti3 MEA is mainly in a stacking-fault-mediated mode rather than the mechanical-twinning-dominated deformation.

3.4. Evolution of deformation substructure in CoCrNi MEA

To obtain a better understanding of the effect of precipitates on the deformation mechanisms, the evolution of deformation substructure of the single-phase CoCrNi MEA was also investigated. Fig. 10 a gives a representative TEM image of the as-recrystallized single-phase CoCrNi MEA. Numerous annealing twins with two types of twin boundaries (indicated by red and yellow lines) were formed (Fig. 10b). The corresponding HRTEM image (Fig. 10c) reveals these two types of twin boundaries belong to $\sum 3\{111\}$ coherent twin boundary (CTB) and $\sum 3\{112\}$ incoherent twin boundary (ITB) with a 9R structure, consistent with the findings in Ref. [15].

Fig. 11 summarizes the microstructural evolution of the CoCrNi MEA deformed to $\sim$2% and $\sim$40% true strain. Fig. 11a shows that at the initial deformation stage ($\sim$2%), a large amount of SFs were formed on {111} planes. When further increasing the strain to $\sim$40%, mechanical twinning was observed as the dominant deformation mode (Fig. 11b and c). SADP pattern clearly demonstrates the existence of twin/matrix (T/M) lamellae in the specimen (see inset in Fig. 11c). Yet the mechanical twins were not so straight as the twins in FeCoNiCrMn HEA[31] and extended SFs were frequently observed within them (an example is shown in Fig. 11d). Interestingly, a large number of non-crystallographic deformation bands with various thicknesses were also formed inside the areas full of twinning lamellae, as shown in the inset in Fig. 11b, which has not been reported in previous investigations on the single-phase CoCrNi MEA.

3.5. Stacking fault energy and deformation modes

The observed substructural evolution in both Al3Ti3 and CoCrNi MEAs is similar to that in the non-cell-forming fcc materials (i.e. planar glide materials) [32]. At the initial

stage of plastic deformation, arrays of dislocation walls (or SFs) were formed along the principal slip directions, a typical planar glide (Fig. 7, Fig. 11). With increasing strain up to failure, the deformation modes in the present two MEAs, however, bifurcated that mechanical twinning became a dominant deformation mode in the single-phase CoCrNi MEA while SFs were favored in the Al3Ti3 MEA. The propensity of mechanical twinning is often thought to be correlated with low SFE [33], [34]. For the CoCrNi MEA, a high propensity of twinning is expected because of a low SFE, 22 ± 4 mJ/m2 [14], comparable to that of high-Mn TWIP steel [35]. The SFE of the matrix in the Al3Ti3 MEA was roughly evaluated based on the findings in Ni-based superalloys [36] and qualitatively compared to the single-phase CoCrNi MEA. According to [36], the addition of Co, Cr, Al and Ti can all somewhat decrease the SFE of Ni-based superalloys while Ni plays the opposite role. Thus, the fcc matrix in the Al3Ti3 MEA should have a lower SFE than the single-phase CoCrNi MEA. We can conclude that the low value of SFE is not the sole factor to dictate twinning propensity [37]. For the Al3Ti3 MEA, there should be another factor influencing the formation of mechanical twinning.

On mechanism of mechanical twinning in fcc materials, it is generally accepted that twinning is initiated by pre-existing dislocations that dissociate into partial dislocations. After the first glide of partial dislocations, requiring the maximum stress, the second glide of partial dislocations takes place on the successive {111} plane. This makes an extrinsic stacking fault, creating an embryo of the mechanical twin. Several dislocation-based models have been proposed for twin nucleation in fcc materials, such as the pole mechanism [38], the pile-up/glide mechanism [39], the homogeneous nucleation mechanism [40] and others [41], all suggesting that deformation twins are created by SFs led by a/6〈112〉Shockley partial dislocations. The preference of twinning and SF

in the deformed materials can be understood by considering the critical stress needed to initiate the Shockley partial dislocation to form a fault loop. Venables [42] proposed a phenomenological relationship between the SFE and the critical twinning stress, where the influence of the SFE on the twinning stress is proportional. However, such phenomenological relation is relatively limited. Swygenhoven et al. [37] have shown that the barrier for twinning lies on the ratio of unstable twinning fault energy to unstable SFE instead of just the intrinsic SFE (refers to the SFE value in almost literature). Furthermore, Rahman et al. [43] discussed the effect of slip length scale on the critical twinning stress, revealing a Hall–Petch type relationship to determine the grain size dependence on critical twinning stress. In our case, however, one should notice that the width of γ phase channel is actually very fine, for example, ~17 nm on average in the CP region estimated with the formula in Ref. [44], which means the source size (D) of dislocation is rather small. According to the classical dislocation theory, Lagerlöf [45] indicated the stress to initiate the Shockley partial dislocation to generate a first stacking fault loop is(1)where μ is the shear modulus, is the Burgers vector of the Shockley partials, is the SFE, and represents the Peierls stress. The parameter α reflects the characteristic of the dislocation (0.5 and 1.5 for edge and screw dislocations, respectively). The shear modulus of the present MEA was assumed to be the same as the single-phase CoCrNi MEA, ~87 GPa [7] and the Burgers vector of the partials is derived from the measured lattice constant from XRD, ~0.146 nm. In Eq. (1), the last two terms associated with the SFE and Peierls stress are independent on the source size, and their summation is assumed to be the critical twinning stress (~260 ± 30 MPa) in CoCrNi MEA with relatively large grain size for simplicity [14]. The first term of the expression depending on the source size is then calculated to be ~2.24 GPa for a γ phase channel with a width of 17 nm. Compared to the flow stress

of the Al3Ti3 MEA, it appears plausible that mechanical twinning is hardly to activate when the width of the γ phase channel is too small. In contrast, when the γ phase channel is wide (in rare cases) twinning can occur since the critical twinning stress is readily reached, as shown in Fig. 9. Another possibility for the missing mechanical twinning is pertinent to the anisotropy of partial dislocation mobility. Azzaz [46] revealed that the larger the anisotropy, the higher the probability for twinning to set in. This can be ruled out since extended SFs are frequently seen in the Al3Ti3 MEA. Also the very fine precipitates may contribute to the absence of mechanical twinning [47] since a certain critical precipitate size is suggested to exist for twinning to occur.

3.6. Strengthening mechanisms

For the Al3Ti3 MEA, possible strengthening mechanisms include solid-solution hardening (), grain size hardening () and precipitation hardening (). And the increase in the yield strength of Al3Ti3 MEA is a simple summation of the individual contributions, expressed as:(2)

Note that the measurement of solid-solution hardening is limited to the traditional dilute alloy system, where dislocation moving is impeded by the strain field arising from the mismatch between the solute and the solvent. However, for HEA or CMCAs, solvent and solute are not distinguishable. In this scenario, the precise evaluation of the solid-solution hardening remains challenging. In the present study, the contribution from solid-solution hardening was experimentally determined as the strength difference between Al3Ti3 MEA under solid-solution state and the single-phase CoCrNi MEA. After performing a tensile test on the solid-solution state of Al3Ti3 MEA, its yield strength (σs) was obtained as ∼334 MPa (the stress-strain curve is not shown). It is important to note that the single-phase CoCrNi MEA has a much fine grain size (∼6.5

μm) compared to the solid-solution state of Al3Ti3 EMA (∼67 μm). To exclude the grain size effect, the yield strength of the CoCrNi MEA with a grain size of 67 μm should be extrapolated. By using the data from Refs. [7], [14] together with our data, the lattice friction (σ0) and strengthening coefficient of *k* for the classical Hall-Petch relationship, $\sigma = \sigma_0 + kd^{-1/2}$ (*d* is the average grain size), are obtained as $\sigma_0 \approx 216$ MPa and $k \approx 568$ MPa μm1/2. Thus, the yield strength (σ67) of CoCrNi MEA with the same grain size (∼67 μm) as the solid-solution-state Al3Ti3 MEA is extrapolated as ∼285 MPa and thus $\Delta\sigma_s = \sigma_s - \sigma_{67}$ should be ∼49 MPa.

DP reaction forms colonies that have different crystallographic orientation with the matrix, which means the original grains will be divided into several small grains, leading to an increase in the strength. In the present work, the grain size decreased to ∼24 μm after DP reaction at 800 °C, and based on the Hall-Petch expression the strength increment from grain size strengthening is ∼46 MPa.

Next, we came to address the last term in Eq. (2), Δσp. The present investigation showed that the precipitates in Al3Ti3 MEA were substantially cut by the glide of dislocations. Therefore, the hardening from precipitates in the Al3Ti3 alloy could be ascribed to (a) stacking-fault strengthening, (b) surface strengthening, (c) coherency strengthening, (d) modulus mismatch strengthening and (e) order strengthening [48]. Here, the first two strengthening mechanisms were ignored since they contribute much less to the total strength of alloys as reported in Ni-based alloys and stainless steel [49], [50]. Furthermore, (c) and (d) occur before the dislocation shears the precipitate and (e) takes place during shearing. Therefore, the increment of strengthening via precipitates can be attributed to the larger of (c) + (d) or (e).

For the CP region with spherical precipitates, the increase in yield strength due to the coherency strengthening mechanism can be calculated following the expression [48]: , where *M*is the Taylor factor (3.06 for a fcc polycrystalline matrix), $\alpha\varepsilon$ is a constant of 2.6 [10], r is the radius of the precipitates, f is the volume fraction of the precipitate and b is the magnitude of the Burgers vector of the matrix ($\sim$0.253 nm). And ε is the matrix-precipitate misfit, defined as , where a is the lattice constant of the matrix and Δa represents the difference of lattice constant between the precipitates and the matrix. Here, Δa was derived from the distance between two planes via HRTEM image and then we could get $\varepsilon \approx 0.2\%$. (d) is caused by the mismatch of shear modulus between the precipitate and the matrix, following an expression as . Here $\Delta\mu$ is the difference of shear modulus between the matrix ($\sim$87 GPa) and the precipitates ($\sim$77 GPa, borrowed from Ni3Al precipitates in Ni-based superalloys [51]), and m = 0.85 [48]. For point (e), the contribution associated with ordering mechanism [48] is , in which γAPB is the antiphase boundary energy. A γAPB of 200 mJ/m2 [44], an intermediate value among the superalloys reported in the literature, is used in the analysis. The other terms have the same significance as defined earlier. Using the above expressions, the values for (c), (d) and (e) were calculated as 134 MPa, 6 MPa and 365 MPa, respectively. As the contribution from (c)+(d) is smaller than (e), the precipitation hardening should be from ordering strengthening. Since flow stress is proportional to hardness [52], here we take an advantage of the hardness ratio of CP region to DP region to deduce the strengthening contribution from DP region. The strengthening contribution from DP region was determined, as $\sim$402 MPa according to the hardness ratio HCP: HDP = 1 : 1.1. Consequently, the overall hardening from precipitates in Al3Ti3 MEA was determined through a simple mixture rule of CP and DP regions, $\sim$388 MPa. Using the above calculations, the yield strength should be

~768 MPa, which is in remarkable agreement with the experimental yield strength of ~750 MPa.

Note that these estimates are somewhat rough since the changes in solute concentration after precipitation (solid-solution strengthening) and the possible changes in coherency strain for precipitates with different size and morphologies (coherency strengthening) were all neglected for simplicity. Furthermore, the relevant parameters, e.g. matrix-precipitate misfit, antiphase boundary energy and modulus difference, were either roughly estimated or adopted from superalloys. More precise evaluations for the contributions from individual mechanisms would require specific knowledge of the strengthening mechanisms and the correlated parameters. Overall, the above analysis suggested that in the Al3Ti3 MEA precipitation hardening plays the dominate role and offers the largest strength increment.

4. Conclusion

In the present work, we fabricated a new precipitation-hardened Al3Ti3 CoCrNi-based MEA with a combination of high strength ~1.3 GPa and a good ductility ~45%. We demonstrated that the minor Ti and Al additions can simultaneously induce both CP (Continuous Precipitation) and DP (Discontinuous Precipitation) reactions. The effect of this heterogeneous precipitation on the deformation behavior of the Al3Ti3 MEA had been investigated and the strengthening mechanisms were discussed. The following conclusions can be made:

•A heterogeneous precipitation behavior was observed in Al3Ti3 MEA by forming two-seam DP colonies, together with a homogeneous precipitation behavior in CP regions. An inspection by STEM, APT and SADPs revealed that those precipitates in both DP and CP regions were the L12 phase.

•Compared to single-phase CoCrNi MEA, the yield strength and ultimate tensile strength of the precipitation-strengthened alloy were significantly increased by ~70% and ~40%, respectively, with a small sacrifice of ductility.

•At the initial stage of the plastic deformation (~2% true strain) in both Al3Ti3 and CoCrNi MEAs, planar dislocations and SFs were activated. And the precipitates in the Al3Ti3 MEA were sheared by paired dislocations and SFs.

•At a high strain level, stacking-fault-mediated process was activated as an additional deformation mechanism in the Al3Ti3 MEA, different from the mechanical twinning observed in the single-phase CoCrNi MEA, even though the SFE of the former is lower than the later. We have revealed that the twinning tendency is not unilaterally determined by the SFE, which also relies on the critical twinning stress impacted by the dislocation source size, e.g. the width of γ phase channel in our case.

•The precipitation hardening (~388 MPa) is devoted significantly to the yield strength of the Al3Ti3 MEA.

Acknowledgments

This work was supported by the Hong Kong Research Grant Council (RGC) for financial support (Grant No. 9380075, 9042048 and 9042204). The APT research was supported by the Collaborative Research Fund (CityU 11205515) from the Research Grant Council, Hong Kong.

References

[1] B. Gludovatz, A. Hohenwarter, D. Catoor, E.H. Chang, E.P. George, R.O. Ritchie, A fracture-resistant high-entropy alloy for cryogenic applications, Science 345 (2014) 1153e1158.

[2] Z. Li, K.G. Pradeep, Y. Deng, D. Raabe, C.C. Tasan, Metastable high-entropy dual-phase alloys overcome the strength-ductility trade-off, Nature 534 (2016) 227e230.

[3] F.X. Zhang, S. Zhao, K. Jin, H. Bei, D. Popov, C. Park, J.C. Neuefeind, W.J. Weber, Y. Zhang, Pressure-induced fcc to hcp phase transition in Ni-based high en- tropy solid solution alloys, Appl. Phys. Lett. 110 (2017) 011902.

[4] Y.F. Ye, Q. Wang, J. Lu, C.T. Liu, Y. Yang, High-entropy alloy: challenges and prospects, Mater. Today 19 (2016) 349e362.

[5] D. Miracle, O. Senkov, A critical review of high entropy alloys and related concepts, Acta Mater. 122 (2017) 448e511.

[6] E. Pickering, N. Jones, High-entropy alloys: a critical assessment of their founding principles and future prospects, Int. Mater. Rev. 61 (2016) 183e202.

[7] Z. Wu, H. Bei, G.M. Pharr, E.P. George, Temperature dependence of the mechanical properties of equiatomic solid solution alloys with face-centered

cubic crystal structures, Acta Mater. 81 (2014) 428e441.

[8] C.P. Lee, C.C. Chang, Y.Y. Chen, J.W. Yeh, H.C. Shih, Effect of the aluminium

content of AlxCrFe1.5MnNi0.5 high-entropy alloys on the corrosion behaviour

in aqueous environments, Corros. Sci. 50 (2008) 2053e2060.

[9] C. Lu, L. Niu, N. Chen, K. Jin, T. Yang, P. Xiu, Y. Zhang, F. Gao, H. Bei, S. Shi, M.R. He, I.M. Robertson, W.J. Weber, L. Wang, Enhancing radiation tolerance by controlling defect mobility and migration pathways in multicomponent

single-phase alloys, Nat. Commun. 7 (2016) 13564.

[10] J.Y. He, H. Wang, H.L. Huang, X.D. Xu, M.W. Chen, Y. Wu, X.J. Liu, T.G. Nieh,

K. An, Z.P. Lu, A precipitation-hardened high-entropy alloy with outstanding

tensile properties, Acta Mater. 102 (2016) 187e196.

[11] W.H. Liu, Z.P. Lu, J.Y. He, J.H. Luan, Z.J. Wang, B. Liu, Y. Liu, M.W. Chen, C.T. Liu,

Ductile CoCrFeNiMox high entropy alloys strengthened by hard intermetallic

phases, Acta Mater. 116 (2016) 332e342.

[12] Y. Zhang, Y. Zhuang, A. Hu, J. Kai, C. Liu, The origin of negative stacking fault

energies and nano-twin formation in face-centered cubic high entropy alloys,

Scr. Mater. 130 (2017) 96e99.

[13] B. Gludovatz, A. Hohenwarter, K.V. Thurston, H. Bei, Z. Wu, E.P. George,

R.O. Ritchie, Exceptional damage-tolerance of a medium-entropy alloy CrCoNi

at cryogenic temperatures, Nat. Commun. 7 (2016) 10602.

[14] G. Laplanche, A. Kostka, C. Reinhart, J. Hunfeld, G. Eggeler, E.P. George, Reasons for the superior mechanical properties of medium-entropy CrCoNi compared

to high-entropy CrMnFeCoNi, Acta Mater. 128 (2017) 292e303.

[15] Z. Zhang, H. Sheng, Z. Wang, B. Gludovatz, Z. Zhang, E.P. George, Q. Yu, S.X. Mao, R.O. Ritchie, Dislocation mechanisms and 3D twin architectures generate exceptional strength-ductility-toughness combination in CrCoNi

medium-entropy alloy, Nat. Commun. 8 (2017) 14390.

[16] R.C. Reed, The Superalloys: Fundamentals and Applications, Cambridge University Press, 2008.

[17] M.S.Lucas,G.B.Wilks,L.Mauger,J.A.Mun~oz,O.N.Senkov,E.Michel, J. Horwath, S.L. Semiatin, M.B. Stone, D.L. Abernathy, E. Karapetrova, Absence of long-range chemical ordering in equimolar FeCoCrNi, Appl. Phys. Lett. 100 (2012) 251907.

[18] D.B. Williams, E.P. Butler, Grain boundary discontinuous precipitation reactions, Int. Met. Rev. (1981) 153e183.

[19] K.N. Braszczyn_x0019_ska-Malik, Discontinuous and continuous precipitation in magnesiumealuminium type alloys, J. Alloys Compd. 477 (2009) 870e876. [20] L. Rayleigh, On the instability of jets, Proc. Lond. Math. Soc. 1 (1878) 4e13. [21] C. Joshi, T. Abinandanan, A. Choudhury, Phase field modelling of rayleigh instabilities in the solid-state, Acta Mater. 109 (2016) 286e291.

[22] A. Perovic, G.R. Purdy, Discontinuous precipitation in Cu-Co alloys, Acta Metall. 29 (1981) 53e64.

[23] J.-O. Andersson, T. Helander, L. Ho€glund, P. Shi, B. Sundman, Thermo-Calc & DICTRA, computational tools for materials science, Calphad 26 (2002) 273e312.

[24] C. Ng, S. Guo, J. Luan, Q. Wang, J. Lu, S. Shi, C. Liu, Phase stability and tensile properties of Co-free Al 0.5 CrCuFeNi 2 high-entropy alloys, J. Alloys Compd. 584 (2014) 530e537.

[25] D.Ma,M.Yao,K.G.Pradeep,C.C.Tasan,H.Springer,D.Raabe,Phasestabilityof non-equiatomic CoCrFeMnNi high entropy alloys, Acta Mater. 98 (2015) 288e296.

[26] B. Geddes, H. Leon, X. Huang, Superalloys: Alloying and Performance, ASM International, 2010.

[27] B.D.Fu,K.Du,G.M.Han,C.Y.Cui,J.X.Zhang,DeformationmechanismsinaCo-rich nickel based superalloy with different size of g0 precipitates, Mater. Lett. 152 (2015) 272e275.

[28] M.C. Chaturvedi, D.J. Lloyd, D.W. Chung, Yielding behaviour of g0-precipitation-strengthened CoeNieCr superalloys, Met. Sci. 10 (2016) 373e378.

[29] V. Gerold, H.P. Karnthaler, On the orgin of planar slip of F.C.C. alloys, Acta

Metall. 37 (1989) 2177e2183.

[30] H. Idrissi, K. Renard, L. Ryelandt, D. Schryvers, P.J. Jacques, On the mechanism of twin formation in FeeMneC TWIP steels, Acta Mater. 58 (2010) 2464e2476.

[31] G. Laplanche, A. Kostka, O.M. Horst, G. Eggeler, E.P. George, Microstructure evolution and critical stress for twinning in the CrMnFeCoNi high-entropy alloy, Acta Mater. 118 (2016) 152e163.

[32] D. Hughes, Microstructural evolution in a non-cell forming metal: Al-Mg, Acta Metall. Mater. 41 (1993) 1421e1430.

[33] K.-T. Park, K.G. Jin, S.H. Han, S.W. Hwang, K. Choi, C.S. Lee, Stacking fault energy and plastic deformation of fully austenitic high manganese steels: effect of Al addition, Mater. Sci. Eng. A 527 (2010) 3651e3661.

[34] K. Youssef, M. Sakaliyska, H. Bahmanpour, R. Scattergood, C. Koch, Effect of stacking fault energy on mechanical behavior of bulk nanocrystalline Cu and Cu alloys, Acta Mater. 59 (2011) 5758e5764.

[35] S. Curtze, V.T. Kuokkala, Dependence of tensile deformation behavior of TWIP steels on stacking fault energy, temperature and strain rate, Acta Mater. 58 (2010) 5129e5141.

[36] X.S. Xie, G.L. Chen, P.J. McHugh, J.K. Tien, Including stacking fault energy into the resisting stress model, Scr. Mater. 16 (1982) 483e488.

[37] H. Van Swygenhoven, P.M. Derlet, A.G. Froseth, Stacking fault energies and slip in nanocrystalline metals, Nat. Mater. 3 (2004) 399e403.

[38] J.A. Venables, On dislocation pole models for twinning, Philos. Mag. 30 (2006) 1165e1169.

[39] J.B. Cohen, J. Weertman, A dislocation model for twinning in f.c.c. metals, Acta Metall. Mater. 11 (1963) 996e998.

[40] M. Yoo, J. Lee, Deformation twinning in hcp metals and alloys, Philos. Mag. A 63 (1991) 987e1000.

[41] S. Mahajan, G. Chin, The interaction of twins with existing substructure and twins in cobalt-iron alloys, Acta Metall. 22 (1974) 1113e1119.

[42] J.A. Venables, Deformation twinning in face-centred cubic metals, Philos. Mag. 6 (1961) 379e396.

[43] K.M. Rahman, V.A. Vorontsov, D. Dye, The effect of grain size on the twin initiation stress in a TWIP steel, Acta Mater. 89 (2015) 247e257.

[44] R.W. Kozar, A. Suzuki, W.W. Milligan, J.J. Schirra, M.F. Savage, T.M. Pollock, Strengthening mechanisms in polycrystalline multimodal nickel-base super-alloys, Metall. Mater. Trans. A 40 (2009) 1588e1603.

[45] K.P.D. Lagerlo€f, J. Castaingy, P. Pirouz, A.H. Heuer, Nucleation and growth of deformation twins: a perspective based on the double-cross-slip mechanism of deformation twinning, Philos. Mag. A 82 (2002) 2841e2854.

[46] M. Zzaz, J.P. Chel, A. Eorge, Plastic deformation, extended stacking faults and deformation twinning in single crystalline indium phosphide 2. S doped InP, Philos. Mag. A 73 (1966) 601e624.

[47] M. Sundararaman, P. Mukhopadhyay, S. Banerjee, Deformation behavior of y00 strengthened inconel 718, Acta Mater. 36 (1988) 847e864.

[48] Ardell, Precipitation hardening, Metall. Trans. A 16A (1985) 1985e2131.

[49] V. Munjal, A. Ardell, Precipitation hardening of Ni-12.19 at.% Al alloy single crystals, Acta Metall. 23 (1975) 513e520.

[50] D. Raynor, J. Silcock, Strengthening mechanisms in g0 precipitating alloys, Met. Sci. J. 4 (1970) 121e130.

[51] T. Pollock, A. Argon, Creep resistance of CMSX-3 nickel base superalloy single crystals, Acta Metall. Mater. 40 (1992) 1e30.

[52] J.R. Cahoon, W.H. Broughton, A.R. Kutzak, The determination of yield strength from hardness measurements, Metall. Trans. 2 (1970) 1971e1979.

Table 1. Chemical compositions of different phases in CP and DP regions of the Al3Ti3 MEA (at. %).

Regions	Phases	Compositions				
		Co	**Cr**	**Ni**	**Al**	**Ti**
CP	Matrix	33.70 ± 0.33	34.42 ± 0.33	28.25 ± 0.31	1.89 ± 0.09	1.75 ± 0.08
	Precipitate	11.30 ± 0.45	3.44 ± 0.23	60.45 ± 0.71	8.92 ± 0.40	15.88 ± 0.53
DP	Matrix	34.81 ± 0.48	37.57 ± 0.62	25.14 ± 0.88	1.53 ± 0.07	0.95 ± 0.16
	Precipitate	14.11 ± 1.19	5.74 ± 1.90	58.19 ± 2.68	9.00 ± 0.33	12.97 ± 0.39

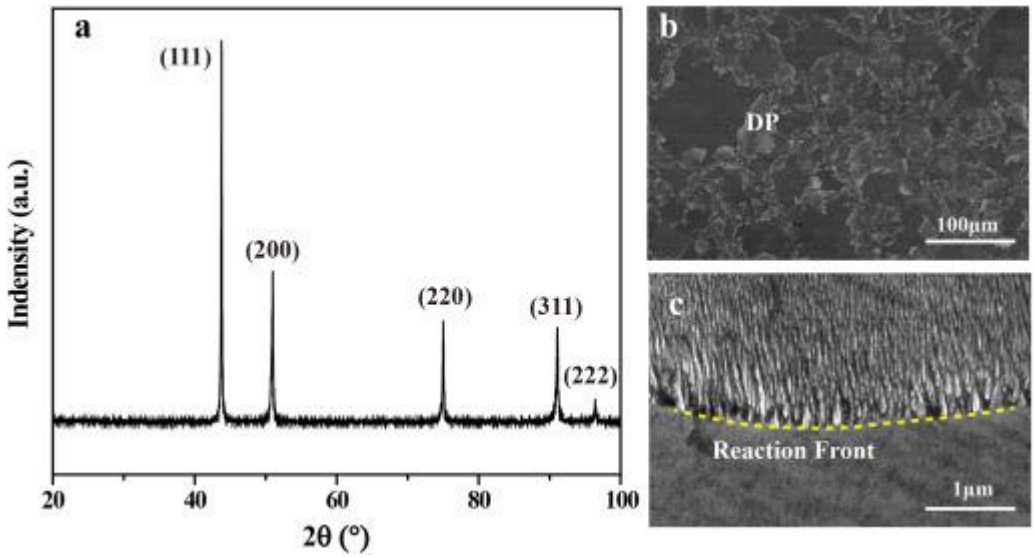

Fig. 1. (a) X-ray diffraction pattern of the Al3Ti3 MEA aged at 800 °C for 2 h. (b) SEM image of a heterogeneous structure resulting from a DP reaction. (c) High-magnification SEM image of the reaction front, highlighted by dashed yellow line. (For interpretation of the references to colour in this figure legend, the reader is referred to the web version of this article.)

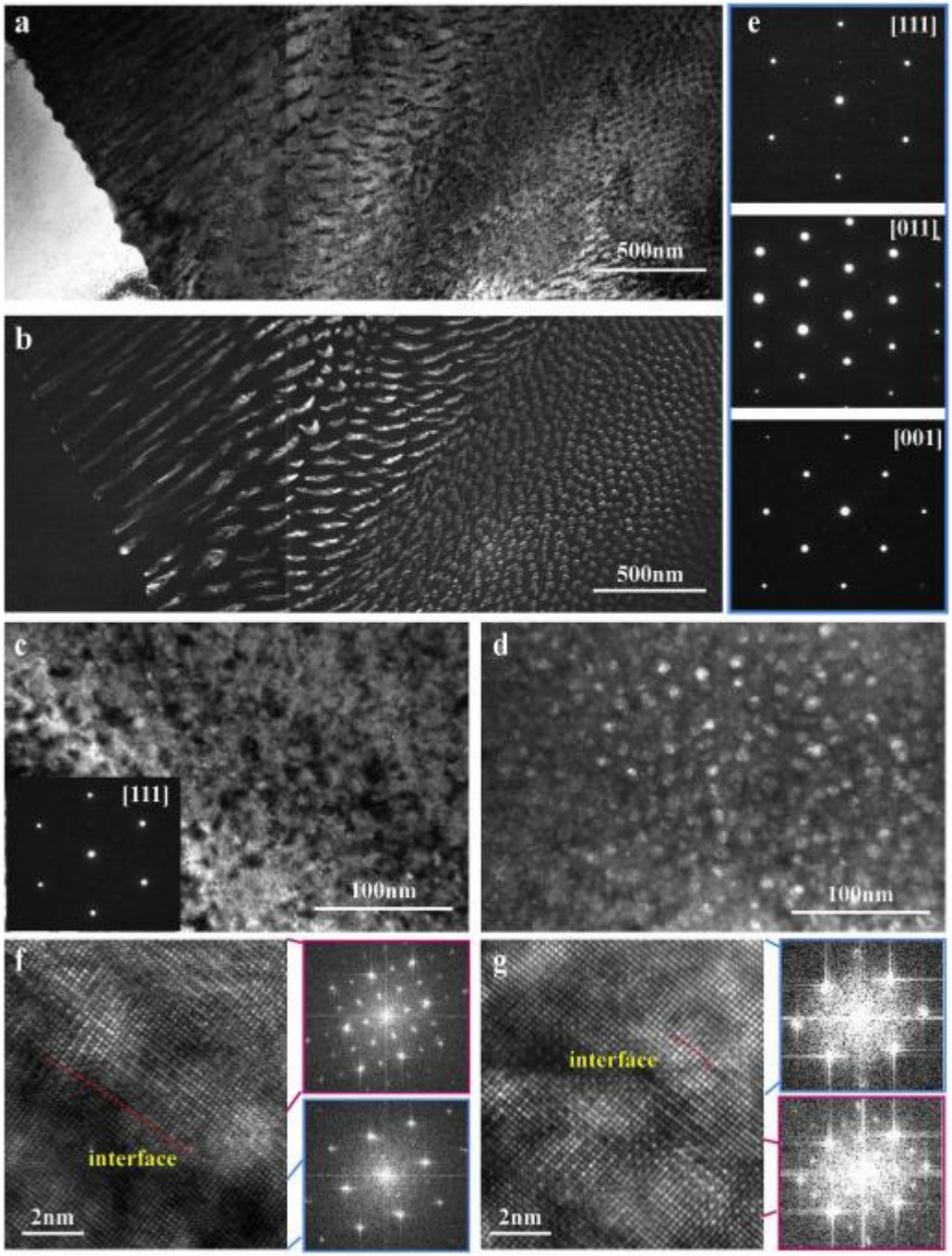

Fig. 2. BF and the corresponding DF TEM images showing the precipitate distribution in CP (a and b) and DP (c and d) regions. (e) SADPs along three zone-axes (z = [111], z = [011] and z = [001]) taken from the DP region. These three SADPs and the inset SADP in (c) demonstrate that the precipitates both in DP and CP regions are γ′ phase with L12 structure. HRTEM images show the precipitate-matrix interfaces in CP (f) and DP (g) regions, with their FFT patterns on their right-hand side.

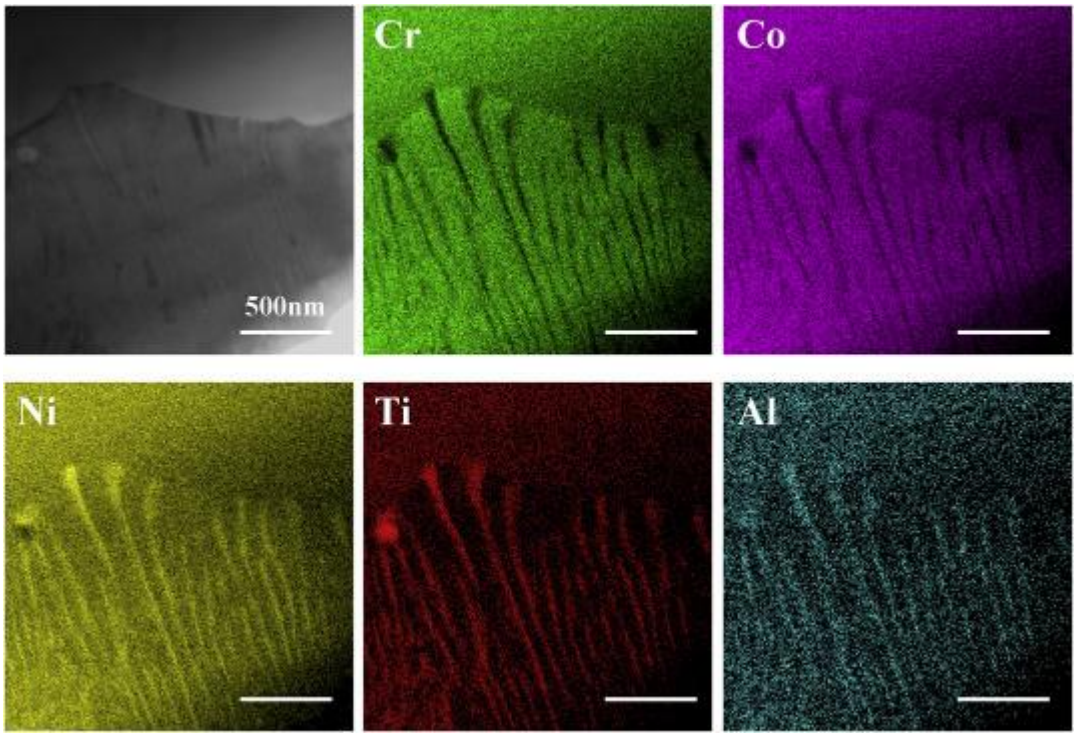

Fig. 3. STEM-EDX elemental mapping of the reaction front of a DP colony.

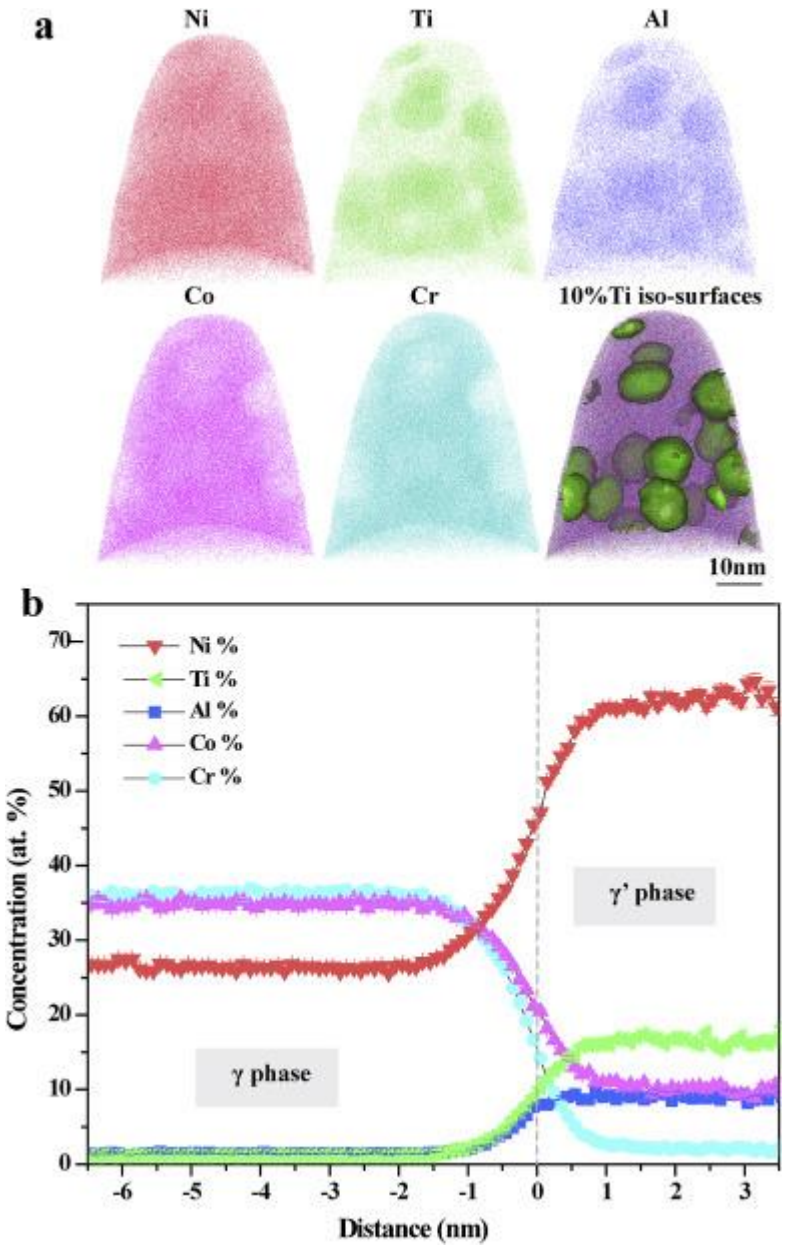

Fig. 4. (a) Ni, Ti, Al, Co and Cr atom maps in a typical APT tip lifted out from CP region and 10 at.% Ti iso-concentration surface showing the outline of precipitates. (b) Proximity histogram of concentration profiles. These results indicate that the L12 particles have the composition of (Ni, Co, Cr)3(Ti, Al).

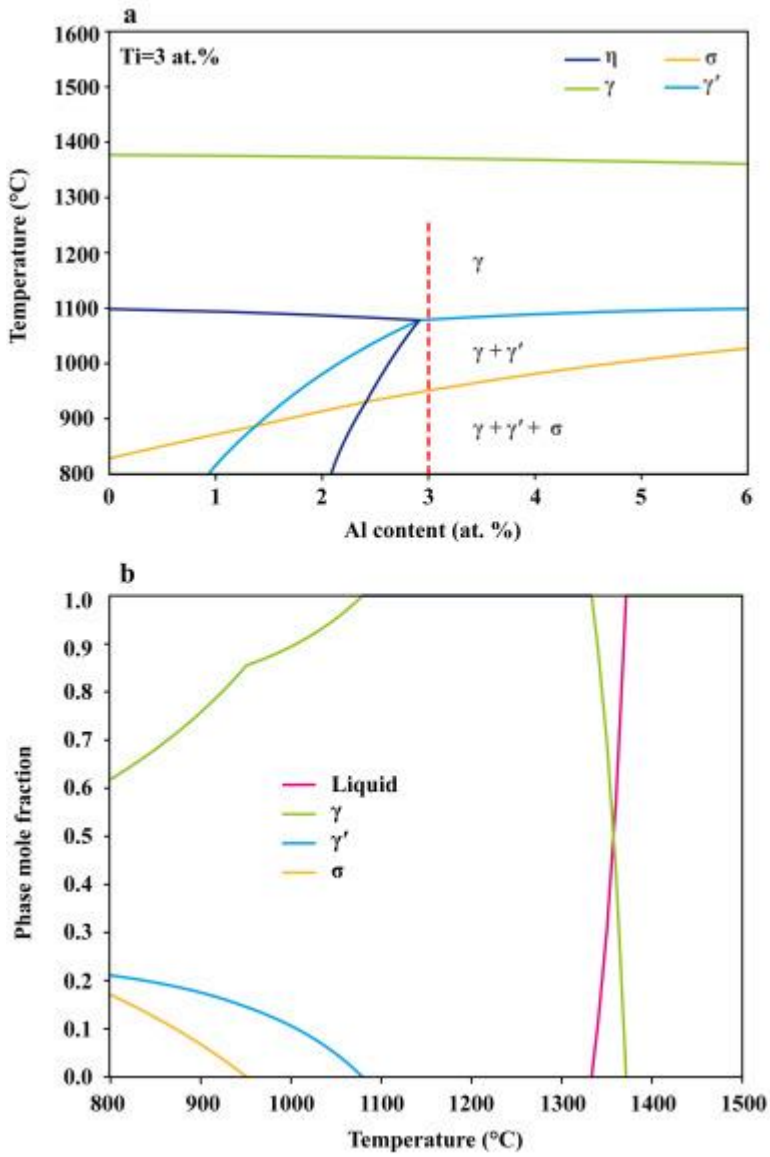

Fig. 5. (a) Phase diagram of the (CoCrNi)97-xTi3-Alx alloy system calculated from Thermo-Cal software with TTNI8 database. (b) The mole fraction of equilibrium phases as a function of temperature.

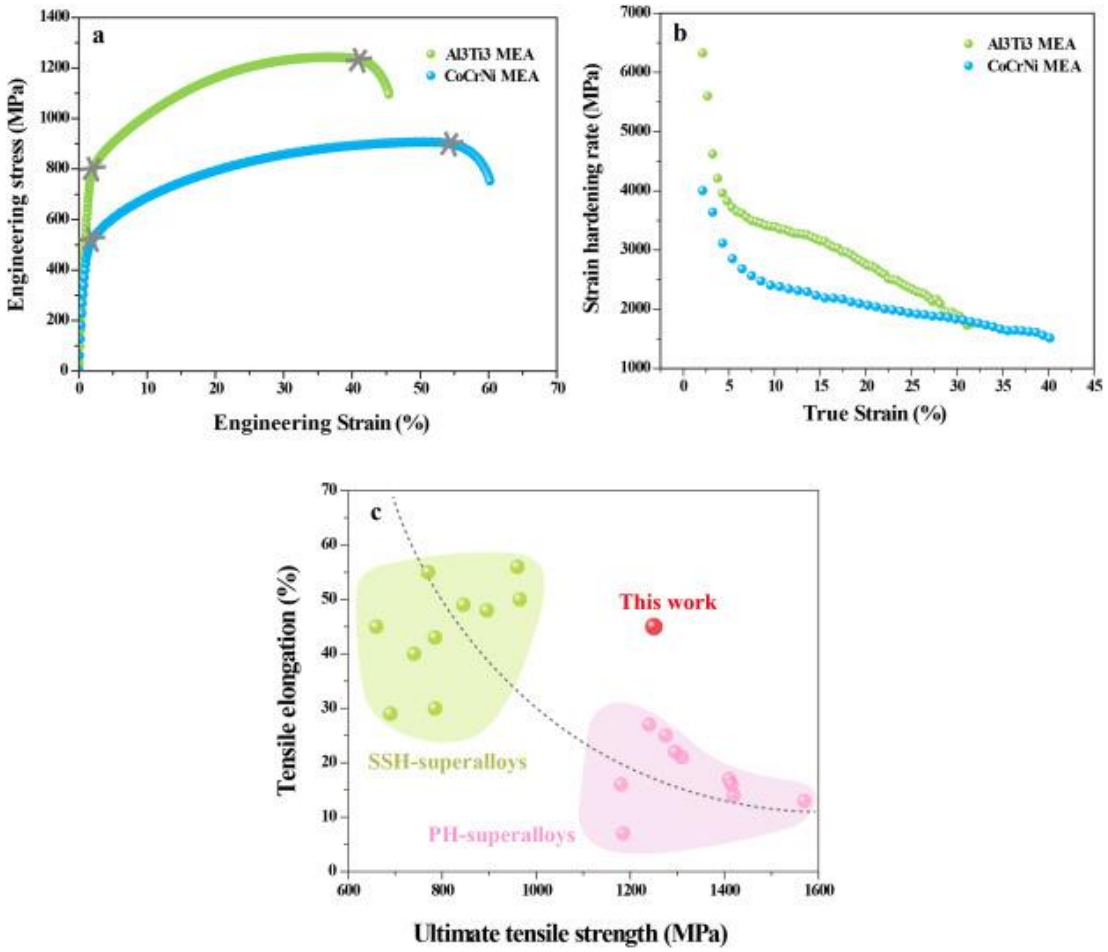

Fig. 6. Engineering stress-strain curves (a) and the corresponding strain hardening rate versus true strain (b) of the CoCrNi and Al3Ti3 MEAs. The grey stars in (a) denote the interrupted test for TEM observation. (c) Ultimate tensile strength versus tensile elongation of the present alloy in comparison with commercial superalloys [26].

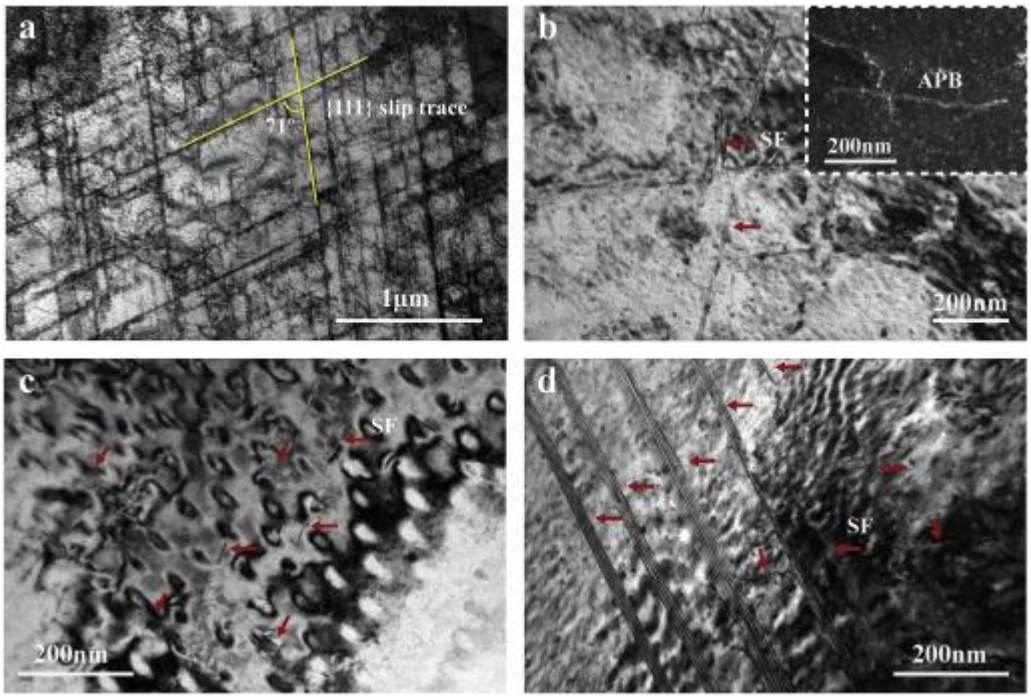

Fig. 7. TEM images showing the microstructures of different regions in the Al3Ti3 MEA after □2% deformation. In the CP region, dislocation slip has a planar characteristic (a) and the precipitates are mainly sheared by SFs and APBs (b); In the DP region, the precipitates are largely deformed by SFs (c) and (d).

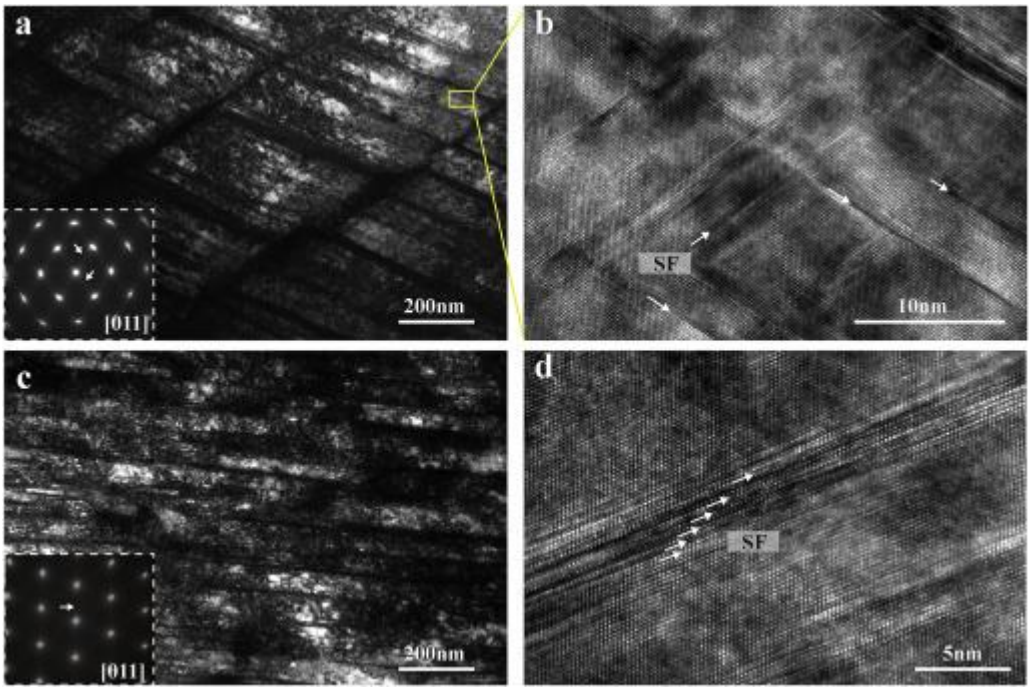

Fig. 8. Prevalence of SFs in the CP (a, b) and DP regions (c, d) of the Al3Ti3 MEA deformed to ~30% true strain. The inserted SADPs are shown to highlight the streaky lines due to edge-on SFs. Representative HRTEM images of the CP and DP region are shown in the (b) and (d), respectively.

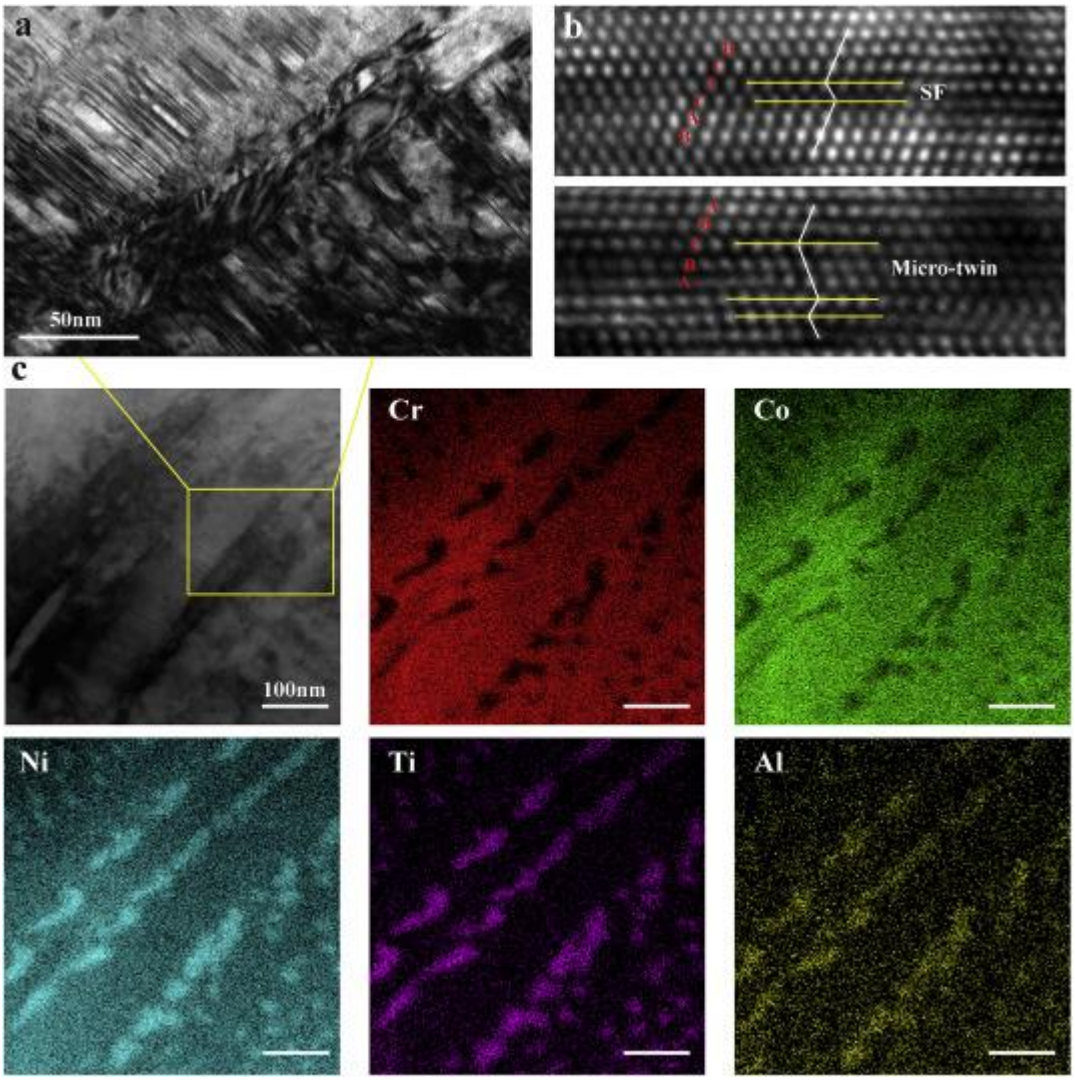

Fig. 9. Further features of substructure in the DP region in the Al3Ti3 MEA sample deformed to □30% true strain. (a) TEMimage, showing a high density of SFs produced within band-like structures. (b) Representative HRTEM images of SF and micro-twin in (a). (c) The corresponding STEM-EDX mapping.

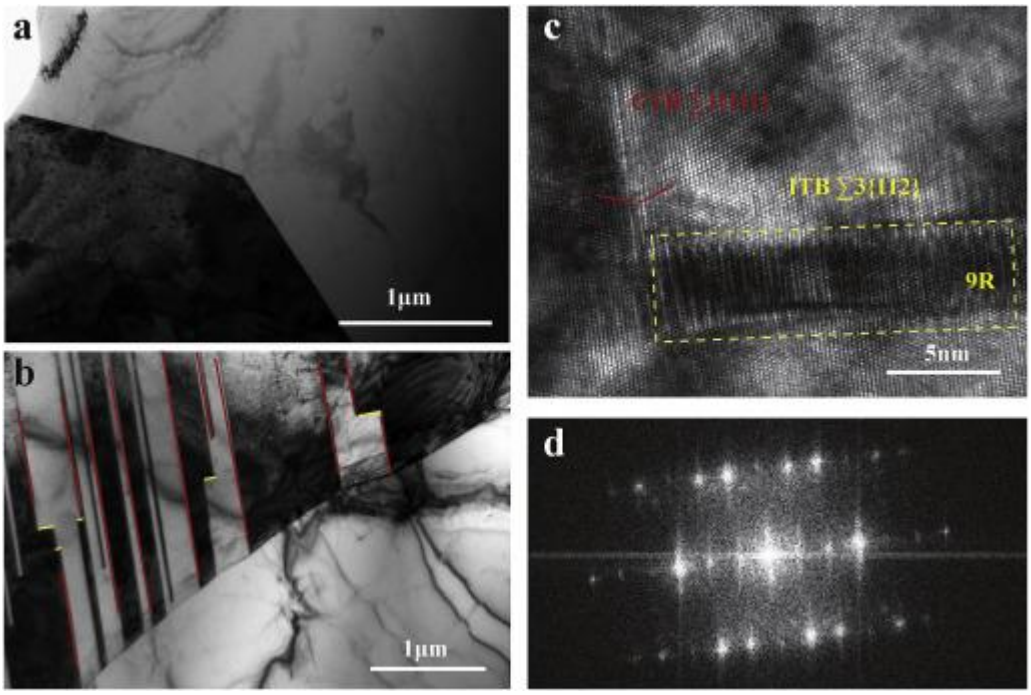

Fig. 10. TEM images of the single-phase CoCrNi MEA in the as-recrystallized state. Low magnification BF images showing the equiaxed grains (a) and numerous annealing twins after recrystallization (b). HRTEM image showing the structure of a CTB and an ITB which contains a 9R structure (c) with the corresponding FFT pattern in (d).

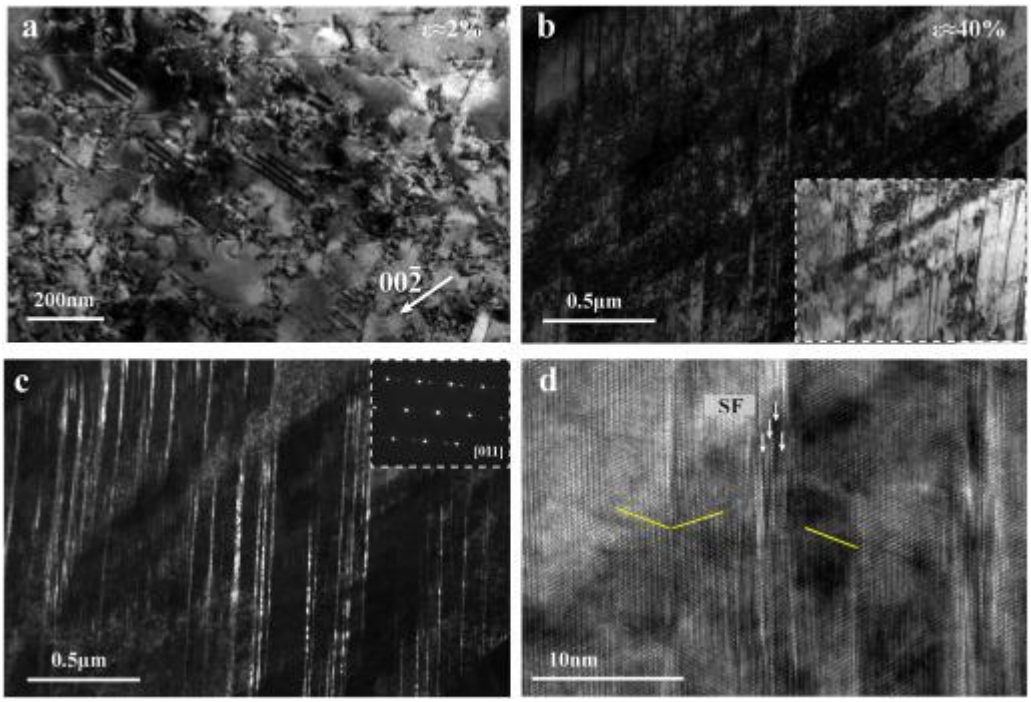

Fig. 11. Twinning dominant deformation mode in the CoCrNi MEA. BF TEM images showing the deformation microstructuresof the single-phase CoCrNi MEA subjected to □2% (a) and □40% (b) deformation. DF image and HETEM of (b) are shown in (c) and (d), highlighting deformation twins.